J. Fluid Mech. (1994), *vol.* 260, *pp.* 247–270

The influence of coherent structures and microfronts on scaling laws using global and local transforms

By L. MAHRT AND J. F. HOWELL
Oceanic and Atmospheric Sciences, Oregon State University, Corvallis, OR 97331 USA

(Received 7 July 1992 and in revised form 5 August 1993)

This study examines the influence of coherent structures and attendant microfronts on scaling laws. Toward this goal, we analyse atmospheric observations of turbulence collected 45 m above a flat surface during the Lammefjord Experiment in Denmark. These observations represent more than 40 hours of nearly stationary strong wind conditions and include more than 1600 samples of the main coherent structures. These samples occupy about 40% of the total record and explain the majority of the Reynolds stress.

To study the dependence of the scaling laws on the choice of basis set, the time series of velocity fluctuations are decomposed into Fourier modes, the local Haar basis set and eigenvectors of the lagged covariance matrix. The three decompositions are compared by formulating joint projections. The decompositions are first applied to the samples of phased-locked coherent structures centred about eddy microfronts. The eigenvector decomposition is able to partially separate the small-scale variances due to the coherent eddy microfronts from that due to the small-scale structure with random phase. In the Fourier spectrum, both of these contributions to the variance appear together at the higher wavenumbers and their individual contributions cannot be separated. This effect is relatively minor for the scale distribution of energy but exerts an important influence on higher-moment statistics. Deviations from the $-\frac{5}{3}$ scaling are observed to be slight and depend on choice of basis set.

The microfronts strongly influence the higher-order statistics such as the sixth-order structure function traditionally used to estimate the energy transfer variance. The intermittency of fine-scale structure, energy transfer variance and dissipation are not completely characterized by random phase, as often assumed, but are partly associated with microfronts characterized by systematic phase with respect to the main transporting eddies. These conclusions are supported by both the higher-order structure function and the higher-order Haar transform.

The Fourier and Haar spectra are also computed for the entire record. The peak of the Haar energy spectrum occurs at smaller scales than those of the Fourier spectrum. The Haar transform is local and emphasizes the width of the events. The Fourier spectrum peaks at the scale of the main periodicity, if it exists, which includes the spacing between the events.

1. Introduction

The following study examines the contribution of coherent structures and intermittent fine-scale turbulence to the scale dependence of the kinetic energy and higher-moment statistics. We will also examine the sensitivity of such scale dependence

to the bases set or statistical tool employed. The Fourier basis set is the most common global basis set and a 'universal language' for comparing different data sets. However, turbulent eddies are local and non-periodic so that the usual Fourier decomposition into Fourier modes can be physically ambiguous as a consequence of Heisenberg's uncertainty principle (Tennekes 1976). This scale ambiguity affects the generalization of the Kolmogorov similarity theory to include the intermittency of dissipation and subsequently allow for modification of the $-\frac{5}{3}$ slope of the Fourier spectrum in the inertial subrange (Kolmogorov 1962; Oboukhov 1962; Novikov & Stewart 1964; Yaglom 1966; Nelkin & Bell 1978).

Similarity scaling arguments have been traditionally interpreted in terms of a continuous energy cascade to smaller and smaller scales which has been questioned in a number of studies (e.g. Frisch, Sulem & Nelkin 1978). As an alternative, large two-dimensional vortices may destabilize directly into three-dimensional structures small enough to contribute to the dissipation (Pierrehumbert & Widnall 1982). This 'short circuit' of the energy cascade was allowed in the arguments of Yakhot, She & Orszag (1989) and is supported by the analysis of Chorin (1982). The short circuit is most commonly posed in terms of non-local interactions in Fourier space (Lesieur 1987). A local reverse transfer of energy to larger scales may occur due to small-scale pairing (Meneveau 1991). Because of the nonlinearity of the non-local interactions, Kraichnan (1974) challenged the concept of universality of modification of the $-\frac{5}{3}$ scaling. With such non-local interactions, the large structures induce anisotropy on the smallest scales (Yeung & Brasseur 1991).

The large eddies may possess concentrated sharp gradients (figure 1 *a*) or microfronts (Chen & Blackwelder 1978; Mahrt 1991*a*) perhaps associated with eddy collision (Morrison & Bradshaw 1991) or outflows from counter-rotating vortices (Blaisdell, Reynolds & Mansour 1991) which lead to near discontinuities. These near discontinuities contribute directly to the energy at high wavenumbers even though they may be an intrinsic feature of the main eddies and associated with changes that are coherent on the main eddy scale. For example, the formation of sharp gradients might be interpreted in terms of convoluted thin vortex sheets (Hunt & Vassilicos 1991). The concentration of fine-scale structure into rods or sheets was inferred by Frisch *et al.* (1978) from the spatial coherency of dissipation.

Even though the sharp gradients are coherent on the larger scales, they contribute to the high-wavenumber energy in the Fourier decomposition and therefore influence the overall slope of the Fourier spectrum (Hunt & Vassilicos 1991). As can be shown by integrating the Fourier transform by parts (Courant & Hilbert 1953), the spectrum is expected to be flatter (relatively more energy at high wavenumbers) when the discontinuities extend to lower-order derivatives. More specifically, the slope of the Fourier spectrum is bounded by the order of the discontinuity. As a possible example, Hunt & Carruthers (1990) note that thin vortex sheets separated by the large-eddy lengthscale contribute to the vorticity at the high wavenumbers. They further argue that in most turbulent flows, linear distortion by the large eddies strongly influences the form of the high-wavenumber spectrum.

The possible formation of singularities due to rapid vorticity accumulation in vortex folds has been discussed in Chorin (1982), Moffatt (1984) and Majda (1991). Majda (1991) further discusses the generation of strong deformation, and therefore strong velocity gradients, by intense vorticity. More specifically, deformation generates vorticity (vortex stretching) while vorticity generates deformation leading to a coupled system capable of producing strong localized vorticity and deformation perhaps approaching singularities.

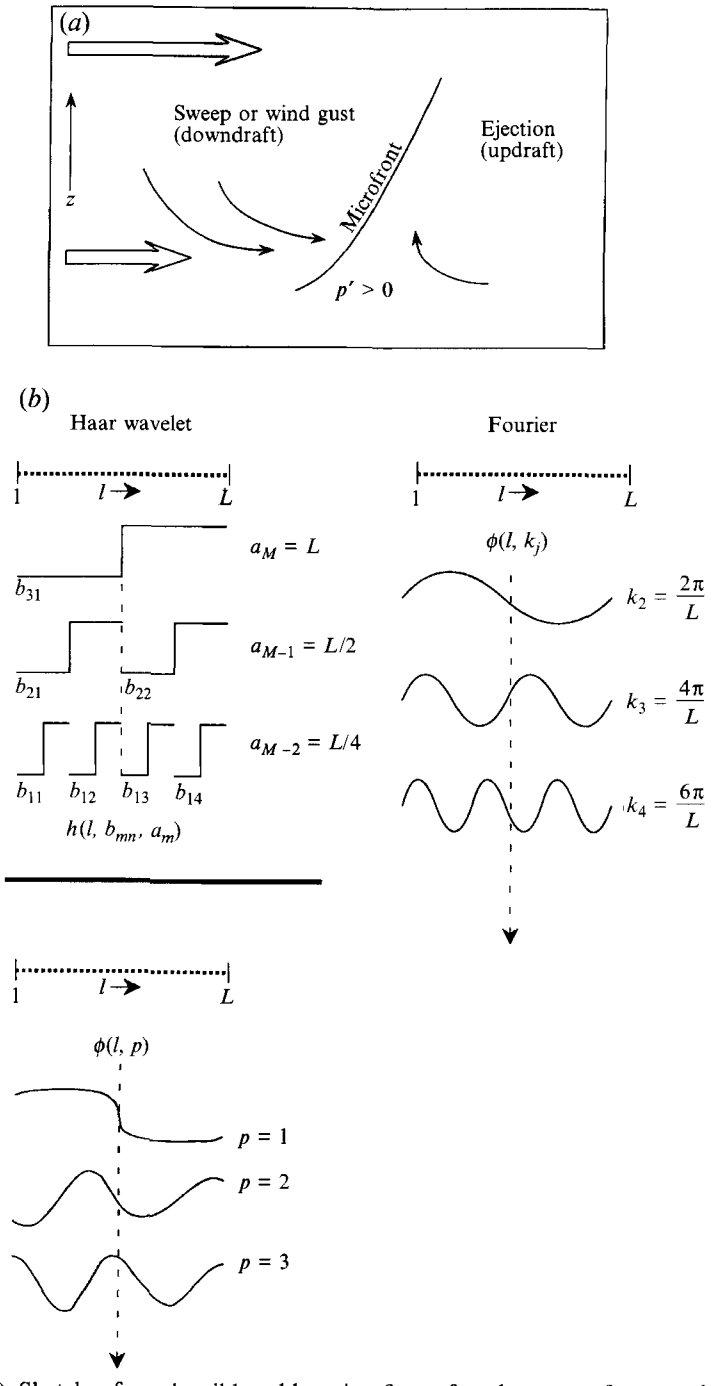

FIGURE 1. (*a*) Sketch of a plausible eddy microfront for the case of mean shear and heating (parentheses). (*b*) The first three basis functions for the different decomposition methods. The eigenvectors are low-resolution versions from the LAMEX data set described in §5.

As another example, Saffman (1971) finds the development of well-separated sharp gradients of vorticity in idealized decaying two-dimensional turbulence which lead to a steep energy spectrum at small wavenumbers, $E(k) \sim k^{-4}$. Sheets of large vorticity

gradients 'accumulate' (Gilbert 1988) leading to a slightly less-steep spectrum between k^{-4} and k^{-3} so that again the role of the discontinuities is to contribute more energy at high wavenumbers and flatten the spectrum. A similar process leads to flattening of the spectrum for three-dimensional turbulence (Moffatt 1984). The dynamical considerations of Yakhot *et al.* (1989) also indicated a slightly flatter spectrum compared to the $-\frac{5}{3}$ slope, as does the B-model of Yamazaki (1990). In contrast, inclusion of fractal intermittency of dissipation (Mandelbrot 1976; Frisch *et al.* 1978) steepens the spectrum in the inertial subrange. The more sheet-like and less convoluted the turbulence, the steeper the spectral slope. Frisch & Morf (1981) pose the bursts of intermittent dissipation in terms of discontinuities resulting from analytical continuation of the Fourier transform onto the complex plane.

The above studies motivate analysis of turbulence time series in terms of near discontinuities and attendant coherent structures. For example, is a significant fraction of the high-wavenumber energy associated with sharp gradients which are a coherent part of larger eddies? Or, are the high-wavenumber part of the Fourier energy spectrum and the higher-moment statistics dominated by fine-scale isotropic turbulence with random phase with respect to the coherent structures? Do the scaling laws and the influence of coherent structures on such scaling laws depend on the choice of basis set?

Motivated by such questions, this study examines scaling laws for samples of phase-locked coherent structures containing microfronts selected from a 40 hour record of turbulence for unusually stationary atmospheric conditions. These scaling laws are compared with those computed for randomly selected samples and those computed for the entire record. The majority of the velocity variance and momentum flux can be explained by the coherent structures containing microfronts. The microfronts appear to be the leading edge of sweeps. The microfronts are not discontinuities and their thickness appears to be large compared to the Kolmogorov scale. Direct eddy simulations, reported in Gerz, Howell & Mahrt (1994), indicate that the microfronts are the leading edge of outflows from counter-rotating vortices. The relationship of microfronts in this study to such vortices, or other types of parent eddies (e.g. Morrison, Subramanian & Bradshaw 1992), cannot be unambiguously determined from the tower data.

After briefly describing the data in the next section, we outline the mathematical definitions of the decompositions (§3). Mapping or transfer matrices between the different decompositions are derived in the Appendix and computed from the data in §4.

2. The data

The data consist of a 40 hour time series of strong, nearly stationary, atmospheric turbulence data (Kristensen *et al.* 1989). Sonic anemometer measurements of the three wind components at 45 m above ground were recorded at 16 Hz. The sonic has a distance constant of 1.2 m which is the effective resolution of the data. While the data provide an unprecedented sample size, the resolution permits examination of only the larger-scale part of the $-\frac{5}{3}$ scaling region. Because of the high Reynolds number, these data still include almost two decades of $-\frac{5}{3}$ scaling. A few atmospheric data sets have been collected with hot-wire measurements which include three to four decades of $-\frac{5}{3}$ scaling; however these data sets are characterized by significant diurnal variation of stability so that only a few hours of data can be analysed with the assumption of quasi-stationarity.

This nearly stationary record of turbulence provides 1680 samples of the main

eddies. With the flow speed averaging about 12.5 m s^{-1} and turbulence depth of roughly 500 m, the Reynolds number is more than 10^8. Estimating the energy dissipation rate from the Kolmogorov scaling law for the $-\frac{5}{3}$ scaling region, with a Kolmogorov constant of 1.5 yields a dissipation rate of 200 cm^2 s^{-3} and a Kolmogorov length of 0.6 mm. The turbulence kinetic energy is 2.1 m^2 s^{-2} corresponding to a velocity scale of about 1.5 m s^{-1} and the stress is 0.5 m^2 s^{-2} corresponding to a surface friction velocity of about 0.7 m s^{-1}. The microscale Reynolds number based on the Taylor microscale is approximately 10^4 while the Reynolds number based on the integral scale for vertical velocity fluctuations is 10^7, where the integral scale is approximately 100 m. The Taylor microscale is estimated to be about 12.5 cm, about an order of magnitude smaller than the resolution of the data. Pseudo-distance is inferred from Taylor's hypothesis using the mean wind speed of 12.5 m s^{-1}. As in Antonia, Satyaprakash & Hussain (1982), we do not make higher-order corrections to this hypothesis. The flow is characterized by zero external intermittency in the sense of Kuznetsov, Praskovsky & Sabelnikov (1992).

During the 40-hour period, the mean wind speed varied from about 13.5 m s^{-1} at the beginning of the period to about 11.5 m s^{-1} at the end of the period. Although unusually stationary for the atmosphere for so long a period, the turbulence kinetic energy decreased by about 30% over the period with some modulation on the timescale of 3–5 hours. The slow trend had no perceptible influence on the scaling laws but did decrease the amplitude of the phase-locked composited structures presented in §5, as inferred by analysing subsegments of the record.

3. Decomposition

The partitioning of the record into phase-locked samples of coherent structures is discussed in §4. In this section, we summarize the methods for decomposition of the samples into orthogonal bases sets needed for the construction of spectra and scaling laws. The decomposition of the sth sample $f_s(x)$ into the basis set for the Fourier modes or the eigenvectors of the lagged covariance matrix can be written as

$$f_s(x) = \sum_{p=1}^{P} W\{f_s, p\}\, \phi[x, p], \tag{1}$$

where $\phi[x,p]$ is the pth orthonormal basis function and the sum is performed over the P basis functions. For the Fourier transform, the basis functions $\phi[x,p]$ are defined as sines and cosines. For the eigenvector bases set (Lumley 1970; Sirovich 1987; Mahrt 1991*a*, *b*), $\phi[x,p]$ is defined in terms of the lagged covariance matrix such that

$$\sum_{l=1}^{L} K(x_l, x)\, \phi[x_l, p] = \lambda(p)\, \phi[x, p], \tag{2}$$

where $K(x_l, x)$ is the lagged covariance matrix, x_l and x are two different relative positions within the sample record and $\lambda(p)$ is the eigenvalue for the pth mode. The first eigenvector maximizes sample covariance-explained, the second eigenvector maximizes explanation of the remaining covariance of the samples and so forth.

The transform coefficients $W\{f_s, p\}$ are defined as

$$W\{f_s, p\} = \sum_{l=1}^{L} \phi[(x_l), p] f_s(x_l), \tag{3}$$

where the sum is defined for a given basis function over the L points in the sample record. The value of the transform is proportional to the amplitude of the structure contained in $f_s(x_l)$ and its similarity to the shape of the basis function.

Each of the Fourier basis functions correspond to a distinct scale (wavelength). The eigenvector basis functions approximately represent decreasing scale with increasing eigenvector number p (§4). In this respect, each of the P basis functions $\phi[x_l, p]$ generates only one transform coefficient $W\{p, f_s\}$ for each scale. In the orthogonal wavelet transform, the basis functions of dilation width a_m points generate L/a_m coefficients for each scale as the transform translates through the record at an incremental distance of a_m. In other terms, the wavelet transform at a given scale generates a number of coefficients representing different neighbourhoods and this number increases with decreasing scale of the basis function. This produces increasing spatial resolution with decreasing scale.

For orthogonal transformations, M dyadic dilation scales are defined such that

$$a_m = 2^m \text{ points}, \quad m = 1, 2 \ldots, M \quad L = 2^M. \tag{4}$$

The smaller-scale basis functions contain higher spatial resolution (figure 1*b*). The actual dilation width is $a_m \Delta x$, where Δx is the distance between points. The transform corresponding to the nth translate begins at the data point

$$b_{mn} = 1 + (n-1)\, a_m; \quad n = 1, \ldots, N \tag{5}$$

so that the first 'translate' ($n = 1$) begins at the first point in the sample and $N = L/a_m$ is the total number of translates equal to $2^{(M-m)}$.

The expansion of the original signal into the wavelet basis set can now be written as

$$f_s(x_l) = \sum_{m=1}^{M} \sum_{n=1}^{N} W\{f_s, a_m, b_{mn}\}\, h[l, b_{mn}, a_m], \tag{6}$$

where $h[l, b_{mn}, a_m]$ is the basis function defined to be non-zero over the points $[b_{mn}, b_{mn} + a_m - 1]$. The wavelet transform $W\{f_s, a_m, b_{mn}\}$ is defined as

$$W\{f_s, a_m, b_{mn}\} = \sum_{l=1}^{L} f_s(x_l)\, h[l, b_{mn}, a_m], \tag{7}$$

where the summation is non-zero over the $a_m = 2^m$ points of the orthogonal transformation where $h[l, b_{mn}, a_m]$ is non-zero.

We choose the Haar basis set (figure 2) written in the form

$$h[l, b_{mn}, a_m] = \left.\begin{array}{rl} -(a_m)^{-\frac{1}{2}}; & 0 \leqslant l - b_{mn} \leqslant (a_m)/2 - 1, \\ +(a_m)^{-\frac{1}{2}}; & (a_m)/2 \leqslant l - b_{mn} \leqslant (a_m) - 1, \\ 0; \quad l < b_{mn}; & l \geqslant b_{mn} + a_m, \end{array}\right\} \tag{8}$$

where l again indicates position within the sample record and b_{mn} is the first point in the transformation window. The normalization by $(a_m)^{-\frac{1}{2}}$ provides the basis set with orthonormality so that

$$\sum_{l=1}^{L} h[l, b_{mn}, a_m]\, h[l, b_{m'n'}, a_{m'}] = \delta_{mm'} \delta_{nn'}, \tag{9}$$

where δ is the Kronnecker delta. The Haar transform is computed by substituting (8) into (7).

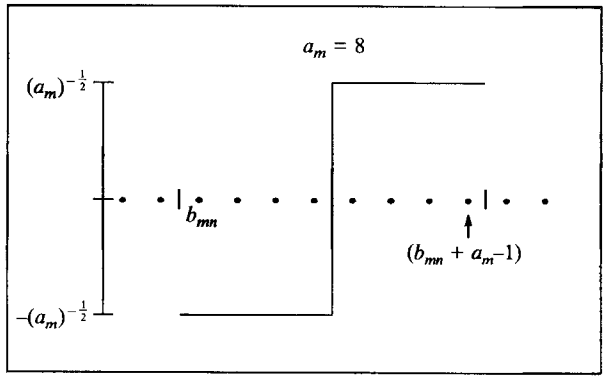

FIGURE 2. The Haar basis function for a single dilation.

The dependence of variance or energy on dilation scale a_m is computed by summing the transform coefficients, at a given scale, over the different translation positions of the transform within each sample record and then additionally averaging over all the samples to obtain

$$\mathrm{Var}[W(a_m)] = \frac{1}{S}\sum_{s=1}^{S}(1/L)\sum_{n=1}^{N} W^2\{f_s, a_m, b_{mn}\}, \tag{10}$$

where the division by L provides computation of the variance. This distribution (10) of variance with scale will be referred to as the wavelet spectrum. Wavelet spectra have been previously computed by Yamada & Ohkitani (1990), Mahrt (1991*a*) and Meneveau (1991).

The projection of the data onto the three different basis sets is constrained by 'transfer matrices' between the basis sets derived in the Appendix. At the same time, the scale dependence for variance in one basis set cannot be used to *a priori* determine the scale dependence in a second basis set. This is partly because the Haar basis is local and omits phase information with respect to absolute position within the record (the implications of this are discussed in §6). Eigenvectors of the lagged covariance matrix and, hence, any associated transfer matrices depend on the data itself.

4. Joint decomposition of the data

4.1. *Sample selection*

We select microfronts, or zones of strong velocity gradients, by choosing samples centred about locations of maximum negative values of the Haar transform (Mahrt & Frank 1988) applied to the longitudinal velocity component. Other conditional sampling techniques seeking sharp gradients yield similar sample sets. The width of the sample records is specified to be about 400 m which optimizes capture of the Reynolds stress. Therefore microfronts are defined here as extrema of the Haar transform on the scale of the main transporting eddies. The composite of the samples selected in terms of regions of maximum momentum flux also exhibit concentrated horizontal velocity gradients centred in the samples, albeit more diffuse than that for samples selected in terms of microfronts. These flux-based samples occupied 50% of the record and explained 96% of the total momentum flux. This high percentage is due to partial cancellation of positive and negative momentum flux occurring between the samples.

The scaling laws are not sensitive to increasing or decreasing the width of the samples, at least within a factor of 2, even though the individual samples change. With

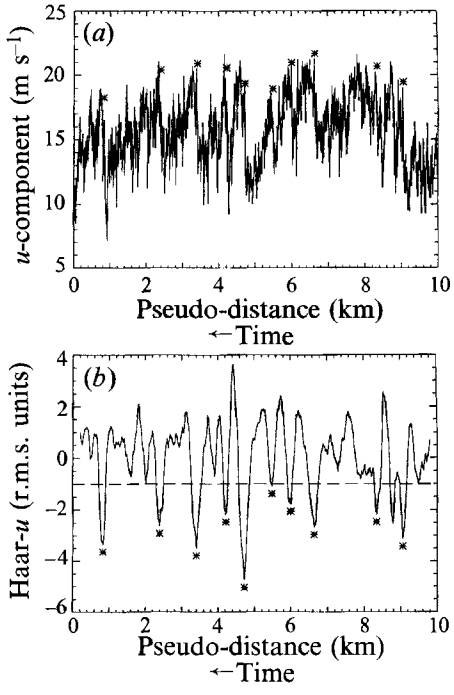

FIGURE 3. (*a*) An example of a time series segment for the longitudinal velocity component, where asterisks indicate centre positions of selected samples and the sample width is 400 m. (*b*) Haar transform time series with transform window width of 400 m, where asterisks indicate sampling based on the Haar transform.

much smaller sample width, sharp changes are still identified but they account for little momentum flux. Increasing the sample width beyond 400 m leads to only gradual increases in the captured stress. For example, doubling the width of the sample records includes about 15% more Reynolds stress and does not appreciably change the form of the scaling laws discussed below. Samples wider than about 1 km include structure from large 'inactive swirling' motions characterized by weak vertical motion and little momentum flux (Townsend 1976). These are the large ramp-like structures on the horizontal scales of a few kilometres (figure 3) which visually are the most organized part of the longitudinal velocity signal and are responsible for the energy maximum in the spectrum for the entire record (figure 10, §6). However these structures exhibit little correlation with the vertical motion field, which is organized on smaller scales of a few hundred metres. Consequently most of the flux occurs on the scale of a few hundred metres which is in the large-scale part of the $-\frac{5}{3}$ scaling region. This feature determines the choice of the 400 m sample record width.

Since the eddies are distorted by the mean shear, the microfronts (figures 1*a* and 3) form mainly at the upstream edges of the slower moving updrafts (bursts) and downstream from faster moving downdrafts (sweeps). As a result, the skewness of the Haar transform of the longitudinal velocity component is negative in pseudo-space (positive in time), averaging -0.33. Samples are selected only at locations where the extreme values of the Haar transform are negative with respect to distance (positive in time) and the absolute value of the Haar transform is larger than its standard deviation. The 1680 samples selected by this procedure occupy 37% of the record and explain about 62% of the total Reynolds stress. While the microfronts generally occur

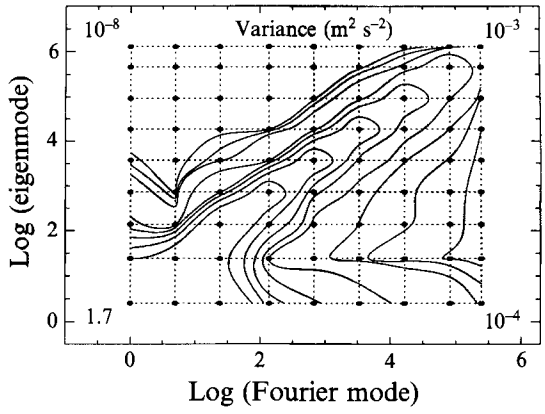

FIGURE 4. The joint decomposition of energy in Fourier wavenumber–eigenvector space for the phase-locked structures. Numerical values at the corner grid points of the joint decomposition are indicated.

at the leading edge of sweeps, a large variety of perturbations on this basic structure occur, at least as seen by the tower data. With stricter sampling criteria formulated in terms of larger values of the Haar transform, the sampled structures are characterized by larger amplitude but occupy a smaller fraction of the record.

For comparison, a second set of samples are selected with no overlap by systematically marching through the record without conditional sampling criteria. These samples are automatically selected with random phase with respect to the coherent structures. Consequently the random-phase samples, as a population, are homogeneous with respect to relative position within the samples, analogous to stationary time series. As a further consequence, the eigenvectors of the lagged correlation matrix for these samples with random phase approach Fourier modes.

4.2. *Fourier and eigenvector decompositions*

The first eigenvector explains 65% of the longitudinal velocity variance within the microfront samples and is characterized by a simple sharp microfront across which the flow decreases sharply in the downstream direction (figures 1*b* and 3), as expected from the sampling criteria. Of importance is that a simple structure can explain a significant fraction of the total variance.

Because of the sharpness of the microfront, the energy associated with the first eigenvector spreads to higher wavenumbers in Fourier space as can be seen from the joint Fourier–eigenvector decomposition† of energy $D^2(j,p)$ defined by (A 18) in the Appendix and plotted in figure 4. As a result, some of the energy decomposed into higher-wavenumber Fourier modes is associated with the microfront and parent eddy as represented by the first eigenvector (lower right corner of figure 4).

In other words, the eigenvector technique is able to separate out the variance due to the narrow microfront edges of the coherent parent eddies from the more random fine-

† Less significant broadening in the joint decomposition occurs at low wavenumbers where a small amount of low-wavenumber energy in the joint decomposition extends to intermediate-order eigenvectors (left side of figure 4). Some of the intermediate eigenvectors are slowly modulated sine waves of intermediate wavenumber and through this modulation contribute some energy to the lowest wavenumbers. The fall-off of the Fourier spectrum at the highest wavenumbers may be influenced by the electronic output filter of the sonic anemometer. The eigenvector spectrum also shows such a fall off, consistent with the fact that the higher order eigenvectors approach Fourier modes.

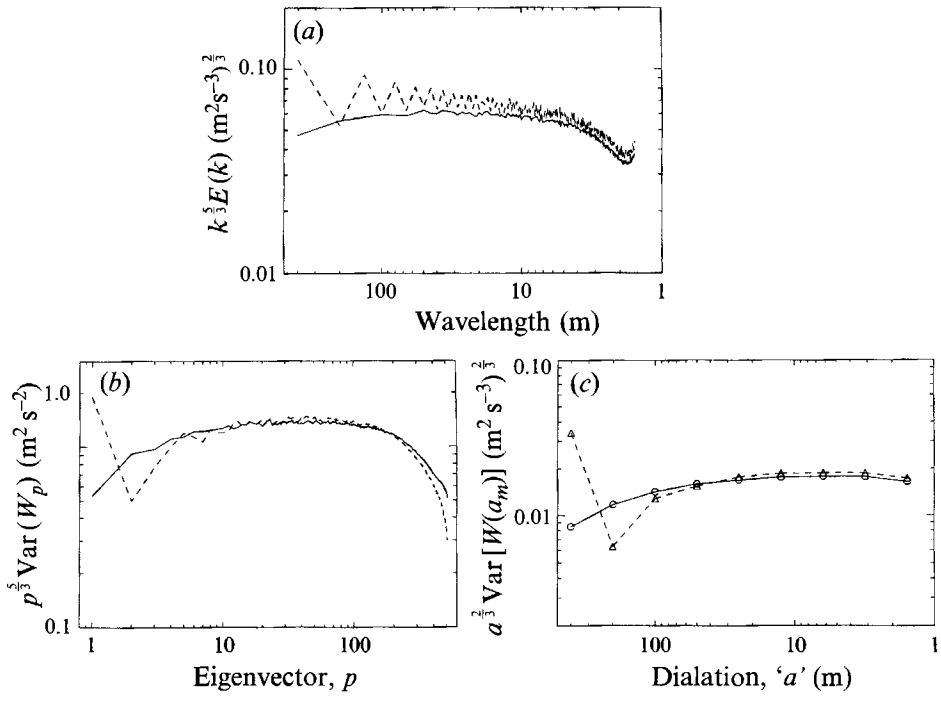

FIGURE 5. The decomposition of variance of phase-locked samples (– – –) and random-phase samples (——) into (*a*) Fourier modes, (*b*) the eigenvectors of the lagged correlation matrix and (*c*) the Haar basis. The spectrum are scaled such that $-\frac{5}{3}$ scaling corresponds to a flat line.

scale structure that appears instead in the higher-numbered eigenvectors. On the other hand in the Fourier decomposition, the energy due to both random fine-scale structure and the eddy microfronts occurs at high wavenumbers in a non-separable way. However, the total contribution of the microfronts to the high-wavenumber energy is relatively modest because the microfronts occupy a small percentage of the total area.

The influence of the spatial inhomogeneity associated with the phase-locked coherent structures is mainly confined to the lowest-order modes (largest scales) for both decompositions. The first few eigenvectors explain a greater percentage of the variance of the coherent structures and capture more of the phase-locked structure than the first few modes of the Fourier expansion (figure 5*a*, *b*). The oscillation of the Fourier spectrum of the phase-locked structures at the low wavenumbers is related to the similarity of the samples to a step change. With a pure step change, the Fourier transform is non-zero only for the odd modes.

Since the intermediate- and higher-order eigenvectors have shapes somewhat similar to trigonometric functions, their projection onto Fourier space is compact (figure 4). Most of the energy in the inertial subrange occurs as an elongated diagonal band in the joint decomposition. Because the main inhomogeneity associated with the phase-locked structures is captured by the first few eigenvectors, the intermediate- and higher-order eigenvectors represent smaller-scale motions with random phase. The eigenvectors for purely random phase motion would be identically Fourier modes. Consequently the eigenvector spectrum (figure 5*b*) obeys the same scaling law as the Fourier spectrum for the inertial subrange. Knight & Sirovich (1990) also found an inertial-subrange scaling law in terms the eigenvector number which obeys the $-\frac{5}{3}$ law when converted to a one-dimensional energy density spectrum.

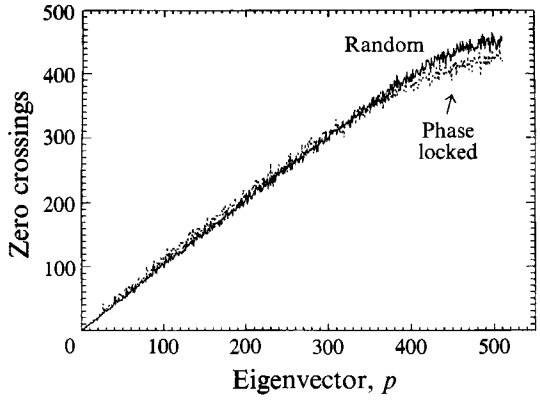

FIGURE 6. The scale of the eigenvectors estimated in terms of the number of zero crossings.

The random phase associated with the intermediate- and higher-order eigenvectors is also reflected by the distribution of the expansion coefficients for the eigenvectors ($W(p, s)$ in (A 12), Appendix) which occur with either sign with equal probability. The random phase in the inertial subrange of the Fourier decomposition is verified by the fact that the observed sine and cosine coefficients of the Fourier expansion are approximately equal. Therefore, the sample records could be approximated by the first few eigenvectors and smaller-wavenumber Fourier components with random phase.

The eigenvector spectrum has been viewed as a scale decomposition since the scale generally decreases with increasing eigenvector number. This systematic variation of scale can be 'measured' by the compact joint eigenvector–Fourier decomposition for higher-order modes (figure 4) or by measuring the scale of the eigenvector in terms of the number of zero crossings (figure 6).

Deviations from the $-\frac{5}{3}$ scaling are minimal. The slope of the Fourier spectrum is steeper than the $-\frac{5}{3}$ value toward the small-scale end of the observed scales, implying that the slope in the interior of the inertial subrange is slightly steeper than $-\frac{5}{3}$ in agreement with Borgas (1992). The slope is slightly flatter than the $-\frac{5}{3}$ value at the large-scale end, probably due to the influence of the large eddies (figure 5*a*). The spectral slope is very close to $-\frac{5}{3}$ for the eigenvector spectrum (figure 5*b*). The slope for the Haar spectrum is slightly flatter than the $-\frac{2}{3}$ value (figure 5*c*). The $-\frac{2}{3}$ slope for the Haar spectrum is equivalent to the $-\frac{5}{3}$ scaling (for further discussion, see Yamada & Ohkitani, 1990 and Meneveau 1991).

The approximate validity of the $-\frac{5}{3}$ scaling for a wide range of scales for the different spectrums of the phase-locked samples and the different spectra of the samples with random phase supports the robustness of this scaling law. In other words, the $-\frac{5}{3}$ prediction seems to be approximately valid independent of the basis sets examined here and occurs in spite of the inhomogeneity of the sample records of coherent structures.

The energy at the largest scales is greater in the phase-locked samples than in the random phase samples owing to the contribution of the coherent structures. The coherent structures do not contain significantly greater small-scale energy than the regions between the coherent structures, indicating that the flow is everywhere fully turbulent. The ratio of the spectral energy for the vertical velocity compared to that for the horizontal velocity (not shown) is 4/3 as predicted by the isotropic theory of longitudinal and transverse correlations (e.g. Tennekes & Lumley 1972, ch. 8.1).

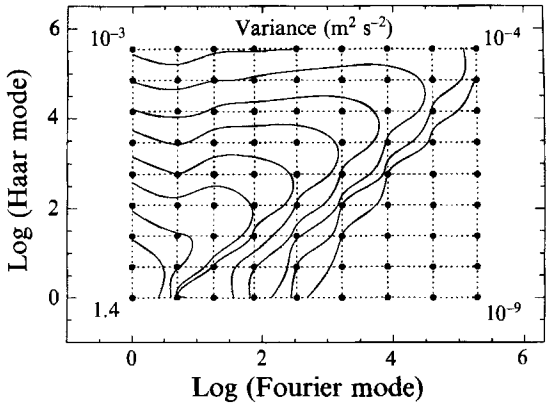

FIGURE 7. The joint decomposition of energy in Fourier–Haar space for the phase-locked structures. Numerical values at the corner grid points of the joint decomposition are indicated.

4.3. *Haar and Fourier spectra*

Compared to the Fourier spectrum, the largest dilation scale of the Haar spectrum (figure 5*c*) contains more energy since it includes more of the variance associated with the phase-locked microfronts (figure 5, 7). As a result, the Haar spectrum exhibits a weak 'spectral gap' between the largest scale representing the phase-locked structure and the smaller-scale more random variance. The weak spectral gap is also related to a relative shift of random-phase energy from larger to smaller scales.† This is evident from the projection of the Haar decomposition onto Fourier space where at low wavenumbers significant joint variance extends to the higher Haar modes (smaller dilation scale) evident in the upper left part of figure 7.

This shift of energy to smaller scales in the Haar decomposition may also explain why the scaling law of the Haar decomposition extends to the smallest measured scales while the energy of the Fourier and eigenvector decompositions decrease faster toward the smallest scales. Counter to this shift, some of the variance associated with the microfront represented by the largest dilation width spreads to intermediate wavenumbers in the Fourier domain (figure 7). However, these shifts in the joint decomposition have little net effect over most of the $-\frac{5}{3}$ scaling range.

4.4. *Scaling laws for orthogonal polynomials and the structure function*

The random and phase-locked structures are also decomposed into orthogonal polynomials. The distribution of variance with polynomial order also exhibits a scaling law that is slightly flatter than $-\frac{5}{3}$ (not shown) which provides more support for the robustness of the $-\frac{5}{3}$ scaling law as an approximation.

† The relative shift of energy to small scales in the Haar decomposition is partly related to the local nature of the Haar transform discussed in §6 and the local bandpass nature of the Haar transform which broadens at smaller scales, as can be deduced from the transfer matrix ((A 10) Appendix).

Even though the first eigenvector captures most of the variance associated with the phase-locked structure, a spectral gap cannot occur in the eigenvector spectrum because each eigenvector maximizes explanation of the remaining variance. However the eigenvector spectrum does exhibit a change of slope at the transition between the lowest modes representing the phase-locked structure and the inertial subrange modes representing more random-phase motion.

In formally comparing the joint decomposition we must note that there are twice as many eigenvectors as Fourier wavenumbers. Each Fourier wavenumber generates two coefficients. In fact the eigenvectors sometimes occur in obvious phase-shifted pairs with sinusoidal-like shape in which case two eigenvector modes approximate one complex Fourier mode.

The structure function does not represent an orthogonal decomposition but is instead an accumulating high-pass filter (Appendix, §A 3). The structure function for these data (not shown) satisfies the $-\frac{2}{3}$ scaling law.

5. Organization of the fine-scale structure by the coherent structures

The organization of the fine-scale structure by the main eddies may be due to advection of small eddies by the larger eddies or generation of small-scale eddies through instability of the shear of the main eddies. The strong gradients concentrated at the microfronts directly contribute to the 'measured' fine-scale structure. The fine-scale structure is traditionally studied in terms of two-point velocity differences. In fact, assuming isotropy at the small scales, the square of the fluctuating divergence $(\delta u/\delta x)^2$ has been used as a one-dimensional surrogate for the local dissipation (Nelkin & Bell 1978) where δu is the two-point difference of the longitudinal velocity over distance δx.

Higher moments of the velocity difference were important indicators of intermittency in the studies of Anselmet, Gagne & Hopfinger (1984), Antonia & Van Atta (1978) and others. We will evaluate the sixth moment of the structure function which serves as an estimate of the fine-scale variability of the energy cascade to smaller scales in the inertial subrange (Frisch *et al.* 1978; Nelkin & Bell 1978, eq. 7; Anselmet *et al.* 1984). If the local dissipation is proportional to the local-scale transfer of energy, then the sixth moment is also a measure of the dissipation variance which in turn increases with intermittency of the dissipation. For the inertial subrange, the energy transfer variance is related to the structure function using the hypothesis of Oboukhov (1962), as in Frisch *et al.* (1978)

$$[\epsilon_l^2(r)] = \frac{1}{L}\sum_{l=1}^{L}[u(x_l+r)-u(x_l)]^6/r^2. \tag{11}$$

Then (11) is averaged over all of the samples and plotted as a function of scale in figure 8.

For scales small compared to the main eddy size, the average energy transfer variance, as estimated from the sixth-order structure function, is expected to approximately follow the similarity law (Nelkin & Bell 1978)

$$\frac{1}{L}\sum_{l=1}^{L}[u(x_l+r)-u(x_l)]^6/r^2 = C_6\,\epsilon^2(r/L^*)^{\zeta_6}, \tag{12}$$

where u is the longitudinal velocity component, L^* is the lengthscale of the main eddies, ϵ is the dissipation rate, C_6 is a non-dimensional coefficient and ζ_6 is a correction to Kolmogorov similarity theory (Nelkin & Bell 1978).

For comparison, the sixth moment of the Haar transform is also computed since the theoretical scaling arguments do not *a priori* dictate the way in which the velocity difference should be computed. The Haar transform is statistically more stable and for a given dilation width is more focused on a given scale (see the Appendix). In terms of the Haar transform, the scaling law assumes the form

$$\frac{1}{L}\sum_{b=1}^{L-a+1}\{(2/a^{\frac{1}{2}})\,W[f_s,a,b]\}^6/(a/2)^2 = C_6^*\,\epsilon^2(r/L^*)^{\zeta_6^*}, \tag{13}$$

where C_6^* and ζ_6^* are companion coefficients to (12), $a = 2r$ and normalization with the factor $(2/a^{\frac{1}{2}})$ is required to pose (13) as differences of averages. As in the calculation of the structure function, the calculation of the Haar transform in this section spatially overlaps. We use all possible scales instead of the orthogonal dyadic set.

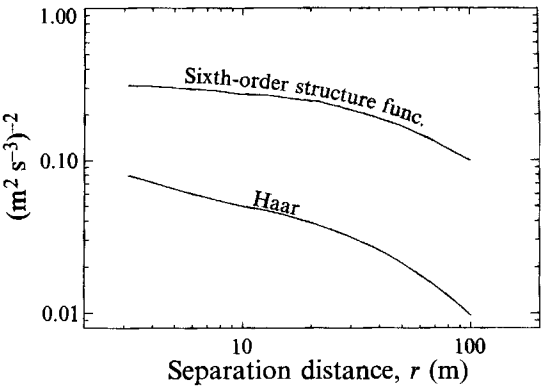

FIGURE 8. Scale dependence of the energy transfer variance estimated in terms of the structure function (11) and the Haar transform (13) for the random-phase samples.

We will analyse only the random phase samples since the similarity relationship (12) is intended for application to stationary signals. Increasing the length of the samples exerts little influence on the scale dependence within the inertial subrange. The energy transfer variance based on the structure function (11) approximately obeys a scaling law with $\zeta_6 = -0.15$ (figure 8).

The scaled energy transfer variance estimated in terms of the Haar transform (13) decreases more rapidly with increasing scale (figure 8) corresponding to a value of ζ_6^* of approximately -0.4. The decrease of energy transfer variance with increasing scale was less when estimated in terms of the structure function because the structure function accumulates variance with increasing separation distance as discussed above. The value of ζ_6^* varies less with scale than the corresponding coefficient for the structure function so that the scaling law is more applicable to the Haar transform. From a more general point of view, the higher-moment statistics depend on the way in which the differences are estimated.

The spatial distribution of the energy transfer variance is estimated by performing a phase-locked composite for different relative positions within the phase-locked samples, that is

$$D_6[x_l, r] = \frac{1}{S}\sum_{s=1}^{S}[f_s(x_l+r) - f_s(x_l)]^6, \tag{14}$$

where the sixth-order velocity difference is averaged over all the samples for a given relative position within the samples, x_l, to form a phase-locked composite. As complementary information we will also compute the phase-locked composite in terms of the Haar transform

$$D_6^*[x_l, a] = \frac{1}{S}\sum_{s=1}^{S}\{(2/a^{\frac{1}{2}})\, W[f_s, a, b]\}^6, \tag{15}$$

where $x_l = b$. Both the structure function and the Haar transform predict the same relative importance of the microfronts (figure 9); the energy transfer variance is strongly concentrated in the microfront zone. While we are unable to directly compute local dissipation, figure 9 suggests that the intermittency of the energy transfer variance is partly related to microfronts. Defining a microfront zone of about 20 m width, the energy transfer variance in the microfront zone is about 20 times larger than outside the microfront zone. The width of the zone of enhanced energy transfer variance is

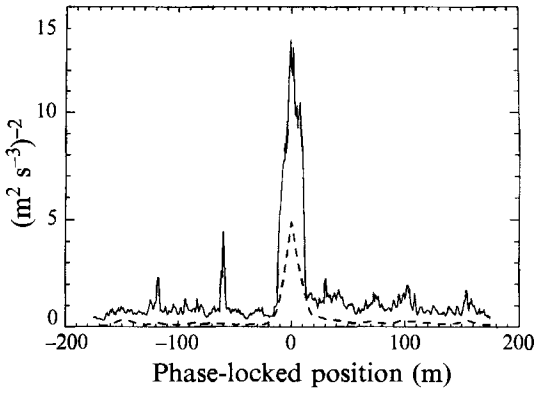

FIGURE 9. Phase-locked composite of the energy transfer variance, estimated in terms of the structure function from (14) (solid line) and the corresponding Haar transform from (15) ($\times 10^2$, dashed line) for $r = \frac{1}{2}a_m = 12$ m.

influenced by the choice of 12 m as the separation distance and has been broadened owing to phase jittering associated with the sample selection and compositing. Since the samples occupy about 40% of the total record, the microfront zones occupy about 2% of the total record and account for about 40% of the total energy transfer variance. Consequently, figure 9 quantitatively indicates that a significant fraction of the small-scale energy transfer variance occurs with systematic phase with respect to the larger-scale structures. This is consistent with (but does not prove) the notion that locations of large production of turbulence are also locations of large dissipation (Kolmogorov 1962); the present study has identified these regions as sharp changes which are associated with coherent spatial structure on the scale of the main transporting eddies.

This situation is somewhat different from the phase-locked composite of horizontal samples across the undulating turbulent–non-turbulent interface constructed by Kuznetsov *et al.* (1992). The interface was characterized by a strong horizontal gradient of the velocity field but the dissipation reached a maximum near the interface, naturally displaced to the turbulent side. In the present study, the turbulence is well developed on both sides of the microfront so that the maximum inferred dissipation is centred on the microfront.

6. Global decomposition of records

The decomposition in §4 projected phase-locked and random-phase samples onto different basis sets. In order to examine the spectra at larger scales and determine the scales of maximum energy, we now decompose the entire record into Fourier and Haar spectra without sampling of events†. This is carried out by first removing the weak

† Since the Haar transform is orthogonal in space, the exact decomposition with respect to the phase of a given coherent structure depends on the starting position of the record. This phase problem can be eliminated by computing the orthogonal Haar decomposition for different starting positions and then averaging the spectra, or, by constructing a complex wavelet basis set as in Grossmann & Morlet (1984), Farge & Rabreau (1988), Grossmann, Kronland-Martinet & Morlet (1989) and Liandrat & Moret-Bailly (1990). This phase problem has little effect on the spectral energy distribution for the present data set because the record is so long.

The Haar wavelet transform can be computed for all possible dilations to provide better scale resolution for estimating the scale of maximum energy. The computation of the Haar transform for

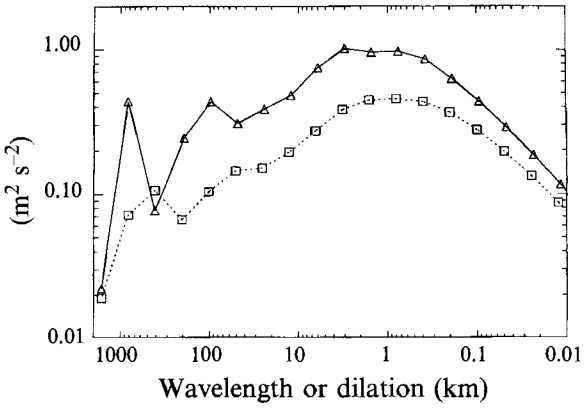

FIGURE 10. Fourier (——△——) and Haar (– – □ – –) spectra for the longitudinal velocity component for the entire record length.

linear trend in the signal and plotting the spectra in log–log coordinates with $kE(k)$ as the vertical coordinate (Tennekes & Lumley 1972). In this case, the $-\frac{5}{3}$ scaling law assumes a $-\frac{2}{3}$ slope.

The Haar and Fourier spectra for the entire record are approximately the same as the spectrum for the random-phase samples for the restricted range of scales covered by the samples (§4). The spectrum for the Fourier decomposition and the Haar decomposition of the longitudinal velocity component have similar shapes (figure 10) although the wavelength of the peak of maximum energy for the Fourier spectrum is approximately two times larger than the dilation of maximum energy for the Haar spectrum. Similar scale shifts occur for the relative minimum and maximum of the spectra at larger scales (figure 10). The Haar spectrum responds more to the width of the structures while the Fourier spectrum corresponds more to the periodicity of such perturbations which includes spacing between the structures. This feature of the Fourier spectrum can be shown using the development of Kharkevich (1960). In contrast the Haar transform is local so that it responds to the width of the events since phase information about the spacing between events is not included (Gamage 1990). This feature was verified by computing the Haar and Fourier spectra for simple artificial records consisting of different building blocks with various spacings. The scale shift of a little more than a factor of two implies that the spacing between the structures averages a little more than the width of the structures. This is consistent with the fact that the structures occupy about 40% of the record.

7. Conclusions and discussion

This study has examined the influence of coherent structures and associated microfronts on scaling laws. The microfronts are loosely defined as zones of concentrated shear and convergence which appear to be the leading edge of downward sweeps. We have selected samples of coherent structures centred about such shear

all possible dilations in concert with the maximum overlap criterion provide transform values for all possible dilation scales a_m and translation positions b_{mn}. Different orthogonal decompositions can be constructed *a posteriori*. Each distinct orthogonal decomposition is related by the kernel of the wavelet transform (Mallat 1989). In the present analysis, we have computed the Haar spectrum only at dyadic scales since better scale resolution was not needed.

zones. Although conditional sampling is never unique, the selected eddies containing the microfronts account for the majority of the momentum flux in the time series. The width of the samples was selected to optimize capture of the momentum flux.

We have computed scaling laws for samples of these eddies as well as for random samples and for the entire record as a whole. Since scaling laws are theoretically argued without reference to specific basis sets, this study sought to estimate the dependence of the observed scaling relationships on the choice of basis set or method of computing gradients. The $-\frac{5}{3}$ scaling law is found to be relatively insensitive to choice of basis set for the energy decomposition, within the ability of the data to define such slopes. This tentative conclusion is based on decomposition of samples of coherent structures into the usual Fourier modes, the local Haar basis set, and eigenvectors of the lagged correlation matrix (EOF's or POF's). The $-\frac{5}{3}$ scaling law in the eigenvector decomposition can be predicted from the observation that the intermediate- and higher-order eigenvectors are each compact in Fourier space and characterized by random phase with respect to the coherent structures. The evaluation of the higher-order eigenvectors was statistically possible in this study because of the very long record length. The decomposition of the variance into the local Haar decomposition also obeys the $-\frac{5}{3}$ scaling.

Since the coherent structures are captured by the lowest-order modes in all three decompositions, the $-\frac{5}{3}$ scaling law at smaller scales is relatively unaffected by the strong spatial inhomogeneity of the phase-locked structures. Consequently, motions with random phase dominate the coefficients of the intermediate- and higher-order modes leading to the $-\frac{5}{3}$ scaling law. The deviations from $-\frac{5}{3}$ scaling are small and depend on the basis set.

The microfronts are captured more efficiently by the lower-order modes in the eigenvector and Haar decompositions as shown in the joint decomposition (§4). Such microfronts contribute to the high-wavenumber energy of the Fourier decomposition in spite of the fact that they are part of the overall structure of the larger coherent structures and thus occur with systematic phase with respect to these eddies. However, the influence of the microfronts on the energy spectrum appears to be relative small owing to the small spatial coverage of the microfronts.

The microfronts exert a much larger influence on higher-order statistics such as the energy transfer variance (sixth-order moment of velocity differences). The narrow microfront zones occupy about 2% of the total record but explain about 40% of the small-scale energy transfer variance. This is a direct measure of the characteristic that the energy transfer variance is less space filling at smaller scales.

When applied to entire records without capturing phase-locked coherent structures, the shape of the Haar and Fourier spectra are similar. However, the maximum energy of the Haar transform occurs at a scale two or three times smaller than the Fourier spectrum. The Haar transform is local so that the energy maximum estimates the width of the main coherent structures. The scale of the energy maximum of the Fourier spectrum is additionally influenced by the spacing between the coherent structures. Thus the two spectra offer complementary information. Since the Haar spectrum can be computed easily and inexpensively, we recommend that it be evaluated as useful supplementary information whenever computing the Fourier spectrum.

Other orthonormal wavelet bases, in addition to the Haar bases, can be applied. We found that smoother wavelet basis functions yielded slightly more extensive scaling regions. However, the choice of the wavelet basis set was not as important as the local character of the basis functions, as previously concluded by Meneveau (1991). The Haar basis was used here because of its simple comparison with the structure function

(A 23), Appendix). Similarly, using different global basis sets, such as the Walsh basis (top-hat trains) produced spectra quite similar to the Fourier spectra.

The computational assistance and comments of Sirlath Desilva and the comments of Nimal Gamage and the reviewers are greatly appreciated. This material is based upon work supported by the USARO under grant DAAL04-93G-0019 and by the Physical Meteorology Program of the National Science Foundation under grant ATM-8912736.

Appendix. Joint projection of covariance between basis sets

A.1. *Notation*

$A(j,p,1), A(j,p,2)$: coefficient for the projection of the pth eigenvector onto the jth Fourier sine mode for variables 1 and 2, respectively;
a: dilation scale in discrete points;
a_m: orthogonal dilation scale in discrete points;
$B(j,p,1), B(j,p,2)$: coefficient for the projection of the pth eigenvector onto the jth Fourier cosine mode for variables 1 and 2, respectively;
b: translate position;
b_{mn}: orthogonal translate position;
C_{mn}: shifted translation position (geometric centre of wavelet transform);
$C^2(j,p) = A(j,p,1)\,A(j,p,2)/2 + B(j,p,1)\,B(j,p,2)/2$;
$D^2(j,p) = \mathrm{Var}(W_p)\,C^2(j,p)$;
$E(k)$: spectral energy density as a function of wavenumber k;
$f_s(x), f_{s1}(x), f_{s2}(x)$: dependent variables for the sth sample or record projected onto the discretized grid;
f_{js}: amplitude of the jth Fourier mode for the sth sample or record;
$h[l, b_{mn}, a_m]$: orthogonal wavelet basis function;
k_j: the jth Fourier wavenumber;
l: position index within sample record, L: total number of points within sample record;
m: index for orthogonal dilation scale, M: total number of orthogonal dilation scales;
n: translation index, N: maximum number of orthogonal translates $= 2^{M-m}$;
p: index for the eigenvector or other global basis set;
q: second index for the eigenvector or other global basis set;
r: separation distance for the structure function;
s: index for sample or record number, S: total number of samples or records;
$\mathrm{Var}(W_p)$: variance explained by pth eigenvector;
$\mathrm{Var}[W(a_m)]$: variance explained by dilation scale a_m in the Haar decomposition;
x: horizontal position;
x_l: discretized horizontal position within sample or record;
$W\{f_s, p\}$: transformation of $f_s(x)$ for pth basis function;
$W\{f_s, a_m, b_{mn}\}$: Haar transformation of $f_s(x)$ for dilation scale a_m and translation b_{mn};
Δx: distance between points;
$\phi[l,p], \phi_1[l,p], \phi_2[l,p]$: eigenvector or other global basis functions.

The scaling laws in different basis sets are related by the transfer matrix between the basis sets. While the relationship between scaling laws in different basis sets cannot be predicted *a priori*, examination of the transfer matrix does put some restrictions on the variation of the scaling laws between the basis sets and provides a formal definition for the joint projections in §4.

A.2. *Joint projection between Fourier and Haar bases*

Using (6), the decomposition of the covariance between two variables $f_{s1}(x)$ and $f_{s2}(x)$ for the sth turbulent structure can be projected onto the Haar basis set as

$$\frac{1}{L}\sum_{l=1}^{L} f_{s1}(x)f_{s2}(x) = (1/L)\sum_{l=1}^{L}\sum_{m=1}^{M}\sum_{n=1}^{N} W\{f_{s1}, a_m, b_{mn}\}\, h[l, b_{mn}, a_m] \times \sum_{m'=1}^{M}\sum_{n'=1}^{N} W\{f_{s2}, a_{m'}, b_{m'n'}\}\, h[l, b_{m'n'}, a_{m'}], \quad \text{(A 1)}$$

where the covariance is computed by summing over the L points in the sample record. Noting that the Haar transform does not depend on l in the above summation and recalling that the basis set is orthonormal, (A 1) assumes the form

$$\sum_{l=1}^{L} f_{s1}(x)f_{s2}(x) = \sum_{m=1}^{M}\sum_{n=1}^{N} W\{f_{s1}, a_m, b_{mn}\}\, W\{f_{s2}, a_m, b_{mn}\}. \quad \text{(A 2)}$$

For decomposition of variance, $f_{s1}(x) = f_{s2}(x)$, (A 2) becomes Parseval's relation for the Haar transform

$$\sum_{l=1}^{L} [f_{s1}(x)]^2 = \sum_{m=1}^{M}\sum_{n=1}^{N} W^2\{f_{s1}, a_m, b_{mn}\}. \quad \text{(A 3)}$$

We now consider the relationship between the above Haar decomposition and the complex discrete Fourier transform. The discrete Fourier basis elements are defined here as

$$e^{ik_j l}, \quad k_j = 2\pi(j-1)/L, \quad i = (-1)^{\frac{1}{2}},$$

where the integers j and l both range from 1 to L where L is again the total number of points in the sample, also equal to 2^M. We write the Fourier decomposition for the sth sample as

$$f_s(x_l) = 2^{-M/2}\sum_{j=1}^{L} f_{js}\, e^{ik_j l}, \quad \text{(A 4)}$$

where the transform coefficients are defined as

$$f_{js} = 2^{-M/2}\sum_{l=1}^{L} f_s(x_l)\, e^{-ik_j l}. \quad \text{(A 5)}$$

Parseval's relation for this expansion is written as

$$\sum_{l=1}^{L} [f_s(x_l)]^2 = \sum_{j=1}^{L} |f_{js}|^2, \quad \text{(A 6)}$$

where $j = 1$ in general represents the mean value of $f_s(x_l)$ which in this case has been removed.

To construct the joint Haar–Fourier decomposition of variance we project the discrete Fourier expansion of $f_s(x_l)$ onto the Haar basis. Substituting the inverse Fourier transform into the Haar transform (7) we obtain

$$W\{f_s, a_m, b_{mn}\} = \sum_{l=1}^{L}\left[2^{-M/2}\sum_{j=1}^{L} f_{js}\, e^{ik_j l}\right] h[l, b_{mn}, a_m], \quad \text{(A 7)}$$

where again $h[l, b_{mn}, a_m]$ is non-zero only over a subinterval of width a_m. After reversing the order of summation and noting that the $j = 1$ term makes no contribution, it follows that

$$W\{f_s, a_m, b_{mn}\} = 2^{-M/2}\sum_{j=2}^{L} f_{js}\left[\sum_{l=1}^{L} h[l, b_{mn}, a_m]\, e^{ik_j l}\right]. \quad \text{(A 8)}$$

The inner sum in (A 8) is the inner product of a wavelet basis element with a Fourier basis element. To evaluate this inner product we note that it is non-zero only over the inclusive interval $[b_{mn}, b_{mn}+a_m-1]$. To simplify the ensuing mathematics we define a translated coordinate l^* so that

$$l = l^* + C_{mn}, \quad C_{mn} = b_{mn} + (a_m/2) - \tfrac{1}{2},$$

where C_{mn} is at the geometric centre of the transformation window. Using (5)

$$C_{mn} = (n-\tfrac{1}{2})\, a_m + \tfrac{1}{2}. \tag{A 9}$$

Applying this coordinate shift and using the definition of the Haar function (8), the inner product in (A 8) can be written as

$$\sum_{l=1}^{L} h[l, b_{mn}, a_m]\, e^{ik_j l} = (e^{ik_j C_{mn}})(a_m)^{-\frac{1}{2}} \left\{ \sum_{l^*=\frac{1}{2}}^{a_m/2-\frac{1}{2}} e^{ik_j l} - \sum_{l^*=\frac{1}{2}-a_m/2}^{-\frac{1}{2}} e^{ik_j l} \right\}.$$

Carrying out the summation, we obtain

$$\sum_{l=1}^{L} h[l, b_{mn}, a_m]\, e^{ik_j l} = (e^{ik_j C_{mn}})(a_m)^{-\frac{1}{2}} i[1-\cos(k_j a_m/2)]/\sin(k_j/2)$$

$$= (e^{ik_j C_{mn}})\, T(k_j, a_m). \tag{A 10}$$

We will refer to $T(k_j, a_m)$ as the transfer matrix.

From (A 8) and (A 10), we obtain

$$W\{f_s, a_m, b_{mn}\} = 2^{-M/2} \sum_{j=2}^{L} f_{js}[(e^{ik_j C_{mn}})\, T(k_j, a_m)]. \tag{A 11}$$

The variance (A 3) can be computed by squaring (A 11), which leads to non-zero cross-terms. These cross-terms are associated with the combination of the local nature of the Haar transform and the global nature of the Fourier transform. For example phase information represented by the factor $e^{ik_j C_{mn}}$ is not contained in the local Haar transform. However (A 11) and the definition of the transfer matrix (A 10) do demonstrate the band-pass nature of the Haar transform. This characteristic is evident in §4 where the joint decomposition between the Haar and Fourier bases were computed using actual data. Since this variance projection cannot be explicitly computed from (A 11), it was instead computed by first decomposing the flow into Fourier modes and then projecting each Fourier mode onto the Haar bases.

A.3. *Joint projection of covariance between Fourier and eigenvector decompositions*

We now formalize the relationship between the eigenvector and Fourier decomposition for the covariance in the discrete case, applied to actual data in §4. The covariance between two variables $f_{s1}(x)$ and $f_{s2}(x)$ for the sth turbulent structure can be projected onto the eigenvector basis set as

$$\frac{1}{L} \sum_{l=1}^{L} f_{s1}(x) f_{s2}(x) = \frac{1}{L} \sum_{l=1}^{L} \sum_{p=1}^{L} \sum_{q=1}^{L} [W(p,s)\, \phi_1(p,l)\, W(q,s)\, \phi_2(q,l)], \tag{A 12}$$

where $W(p,s)$ and $W(q,s)$ represent the expansion coefficients for the pth and qth eigenvectors, respectively, and $\phi_1(p,l)$ is the pth eigenvector for the first variable and $\phi_2(q,l)$ is the qth eigenvector for the second variable. The total number of eigenvectors is equal to L, the number of points in the sample records.

The eigenvectors for two or more variables can be computed simultaneously by staking variables into one observational vector to study the total lagged covariance

between the variables. Then $\phi_1(p,l)$ and $\phi_2(q,l)$ are the parts of the same eigenvector associated with $f_{s1}(x)$ and $f_{s2}(x)$, respectively, and the expansion coefficient $W(p,s)$ applies to the entire eigenvector. In the data analysis of §4, we examine the joint decomposition of the variance of the longitudinal velocity component in which case $f_{s1}(x) = f_{s2}(x) = u(x)$.

To compute the total covariance for the population of sampled structures, we average (A 12) over the S samples and note that the expansion coefficients for the different eigenvectors are uncorrelated. We then obtain

$$\frac{1}{S}\sum_{s=1}^{S}\frac{1}{L}\sum_{l=1}^{L} f_{s1}(x) f_{s2}(x) = \sum_{p=1}^{L} \mathrm{Var}(W_p) \sum_{l=1}^{L} \phi_1(p,l)\,\phi_2(p,l), \tag{A 13}$$

$$\mathrm{Var}(W_p) = \frac{1}{SL}\sum_{s=1}^{S} W^2(p,s). \tag{A 14}$$

The covariance for a given eigenvector is proportional to the energy attributed to the eigenvector, as represented by the square of the expansion coefficient (A 14). The covariance is also proportional to the correlation between the two parts of the eigenvector corresponding to the respective variables in the covariance.

For comparison, the eigenvector decomposition can be projected onto a more traditional basis set (Sirovich 1987) such as sines and cosines. The decomposition of the pth eigenvector for variables $f_{s1}(x)$ into a Fourier series can be written as

$$\left.\begin{aligned} &\phi_1(p,l) = \sum_{j=1}^{L} A(j,p,1)\sin(k_j l) + B(j,p,1)\cos(k_j l), \quad l = 1,\ldots,L, \\ &k_j = 2\pi(j-1)/L, \end{aligned}\right\} \tag{A 15}$$

where here $A(j,p,1)$ and $B(j,p,1)$ are the coefficients of the Fourier series for the pth eigenvector for variable 1 and L is the number of points in the sample records. Substituting (A 15) and the analogous expression for $f_{s2}(x)$ into the expression for within-sample covariance (A 13), we obtain

$$\frac{1}{S}\sum_{s=1}^{S}\frac{1}{L}\sum_{l=1}^{L} f_{s1}(x) f_{s2}(x) = \sum_{p=1}^{L} \mathrm{Var}(W_p) \sum_{j=1}^{L} \left\{\sum_{l=1}^{L} A(j,p,1)\sin(k_j l) + B(j,p,1)\cos(k_j l)\right\}$$
$$\times \left\{\sum_{l=1}^{L} A(j,p,2)\sin(k_j l) + B(j,p,2)\cos(k_j l)\right\}. \tag{A 16}$$

Applying the orthogonality of the sine and cosine modes when averaged over the sampled structure, (A 16) becomes

$$\frac{1}{S}\sum_{s=1}^{S}\frac{1}{L}\sum_{l=1}^{L} f_{s1}(x) f_{s2}(x) = \sum_{p=1}^{L} \mathrm{Var}(W_p) \sum_{j=1}^{L} C^2(j,p) = \sum_{p=1}^{L}\sum_{j=1}^{L} D^2(j,p), \tag{A 17}$$

where

$$C^2(j,p) = A(j,p,1)\,A(j,p,2)/2 + B(j,p,1)\,B(j,p,2)/2,$$
$$D^2(j,p) = \mathrm{Var}(W_p)\,C^2(j,p). \tag{A 18}$$

$D^2(j,p)$ represents covariance of the pth eigenvector described by the jth Fourier mode and $C(j,p)$ is a transfer matrix. In the data analysis of this study, we will decompose the variance so that $f_{s2}(x) = f_{s1}(x)$. Then the product $A(j,p,1)\,A(j,p,2)$ reduces to $A^2(j,p,1)$ and so forth. The sum

$$\sum_{j=1}^{L} D^2(j,p) \tag{A 19}$$

is the spectrum (or cospectrum) based on the eigenvector basis set and is computed from the data in §4.

The Fourier cospectrum can be recovered by noting that $\mathrm{Var}(W_p)$ is independent of the Fourier wavenumber and switching the order of summation in (A 17), in which case we obtain

$$\frac{1}{S}\sum_{s=1}^{S}\frac{1}{L}\sum_{l=1}^{L}f_{s1}(x)f_{s2}(x)=\sum_{j=1}^{L}C_j^2,$$

where

$$C_j^2=\sum_{p=1}^{L}\mathrm{Var}(W_p)\,C^2(j,p).$$

This decomposition of variance in the Fourier spectral domain relates the covariance in each Fourier mode to the contributions from the P different eigenmodes. Therefore the projections (A 17)–(A 19) show the relationship between the scale dependence based on the eigenvector decomposition and the scale dependence based on the Fourier modes, which is evaluated from actual data in the joint decomposition in §4.

A.4. Scaling laws for the structure function and Haar bases

The averaging over the two halves of the Haar transform partially removes the influence of smaller scales while the structure function is influenced by variations on all scales smaller than r. That is the Haar transform is equivalent to averaging $f(x_l)$ over the two half-widths of the transformation window, and then computing the difference between these two means. To explicitly show the relationship between the structure function and the Haar transform, we define the deviation from the half-window means, $f'(x_l)$ and $f'(x_l+r)$, and express the half-window means in terms of the Haar transform so that

$$f(x_l)=f'(x_l)+h(2r,x_l)\,W(2r,b),\quad f(x_l+r)=f'(x_l+r)+h(2r,x_l+r)\,W(2r,b),\tag{A 20}$$

$$h(2r,x_l)=-(a)^{-\frac{1}{2}}=-(2r)^{-\frac{1}{2}},\quad h(2r,x_l+r)=+(2r)^{-\frac{1}{2}},\tag{A 21}$$

and $W(2r,b)$ is the coefficient of the Haar transform for a single dilation $2r$, and b is again the first point of the Haar transform window. The structure function is computed over the same domain as the Haar transform window by incrementing the position of the two-point difference one point at a time. Then using (A 20), the structure function becomes

$$\frac{1}{r}\sum_{l=1}^{r}[f(x_l+r)-f(x_l)]^2=\frac{1}{r}\sum_{l=1}^{r}\{[f'(x_l+r)+h(2r,x_l+r)\,W(2r,b)]-[f'(x_l)+h(2r,x_l)\,W(2r,b)]\}^2.\tag{A 22}$$

We carry out the multiplication on the right-hand side and note that $h(2r,x_l)$, $h(2r,x_l+r)$, and $W(2r,b)$ are all constant over each half-window so that all terms that are linear in $f'(x_l)$ or $f'(x_l+r)$ sum to zero. Then (A 22) becomes

$$\frac{1}{r}\sum_{l=1}^{r}[f(x_l+r)-f(x_l)]^2=2W^2(2r,b)+\frac{1}{r}\sum_{l=1}^{r}[f'(x_l+r)-f'(x_l)]^2.\tag{A 23}$$

Therefore the structure function can be written as the Haar estimate of the square of the velocity difference plus a contribution due to variations on scales smaller than the separation distance r (second term on the right hand side of (A 23)).

By expanding $f'(x_l)$ and $f'(x_l+r)$ in terms of the Haar basis, one can show that the scaling law for dependence of variance on scale in terms of the Haar transform is

related to the scaling law for the structure function. Indeed, the structure function and the corresponding Haar calculation for the phase-locked samples and the random samples both show approximate $-\frac{2}{3}$ scaling. However, the higher-moment calculations are more sensitive to the way differences are computed and to the occurrence of phase-locked structure, as shown in §5.

REFERENCES

ANSELMET, F., GAGNE, Y. & HOPFINGER, E. J. 1984 High-order velocity structure functions in turbulent shear flows. *J. Fluid Mech.* **140**, 63–89.

ANTONIA, R. A., SATYAPRAKASH, B. R. & HUSSAIN, A. K. M. F. 1982 Statistics of fine-scale velocity in turbulent plane and circular jets. *J. Fluid Mech.* **119**, 55–89.

ANTONIA, R. A. & VAN ATTA, C. W. 1978 Structure functions of temperature fluctuations in turbulent shear flows. *J. Fluid. Mech.* **84**, 561–580.

BLAISDELL, G. A., REYNOLDS, W. C. & MANSOUR, N. N. 1991 Compressibility effects on the growth and structure of homogeneous turbulent shear flow. In *Eighth Symp. on Turbulent Shear Flows*, Vol. 1, pp. 111–116. Tech. Univ. of Munich.

BORGAS, M. S. 1992 A comparison of intermittency models in turbulence. *Phys. Fluids* A **4**, 2055–2061.

CHEN, C. H. P. & BLACKWELDER, R. F. 1978 Large-scale motion in turbulent boundary layer: A study using temperature contamination. *J. Fluid Mech.* **89**, 1–31.

CHORIN, A. J. 1982 The evolution of a turbulent vortex. *Commun. Math. Phys.* **83**, 517–535.

COURANT, R. & HILBERT, D. 1953 *Methods of Mathematical Physics*, Vol. 1. Interscience.

FARGE, M. & RABREAU, G. 1988 Transformée en ondelettes pour détecter et analyser les structures cohérentes dans les écoulements turbulents bidimensionnels. *C.R. Acad. Sci. Paris* **307**, (II), 1479–1486.

FRISCH, U. & MORF, R. 1981 Intermittency in nonlinear dynamics and singularities at complex times. *Phys. Rev.* A **23**, 2673–2705.

FRISCH, U., SULEM, P. L. & NELKIN, M. 1978 A simple dynamical model of intermittent fully developed turbulence. *J. Fluid Mech.* **87**, 719–736.

GAMAGE, N. K. K. 1990 Modeling and analysis of geophysical turbulence: Use of optimal transforms and basis sets. PhD thesis, Oregon State University.

GERZ, T., HOWELL, J. & MAHRT, L. 1994 Vortex structures and microfronts. *Phys. Fluids* A (submitted).

GILBERT, A. D. 1988 Spiral structures and spectra in two-dimensional turbulence. *J. Fluid. Mech.* **193**, 475–497.

GROSSMANN, A., KRONLAND-MARTINET, R. & MORLET, J. 1989 Reading and understanding continuous wavelet transforms. In *Wavelets: Time-Frequency Methods and Phase Space* (ed. J. M. Combes *et al.*), pp. 1–20. Springer.

GROSSMANN, A. & MORLET, J. 1984 Decomposition of Hardy functions into square integrable wavelets of constant shape. *SIAM J. Math. Anal.* **15**, 723–736.

HUNT, J. C. R. & CARRUTHERS, D. J. 1990 Rapid distortion theory and the 'problems' of turbulence. *J. Fluid Mech.* **212**, 497–532.

HUNT, J. C. R. & VASSILICOS, J. C. 1991 Kolmogorov's contributions to the physical and geometrical understanding of small-scale turbulence and recent developments. *Proc. R. Soc. Lond.* A **434**, 183–210.

KHARKEVICH, A. A. 1960 *Spectra and Analyses.* Consultants Bureau.

KNIGHT, B. & SIROVICH, L. 1990 Kolmogorov inertial range for inhomogeneous turbulence flows. *Phys. Rev. Lett.* **65**, 1356–1359.

KOLMOGOROV, A. N. 1962 A refinement of previous hypotheses concerning the local structure of turbulence in a viscous incompressible fluid at high Reynolds number. *J. Fluid Mech.* **13**, 82–85.

KRAICHNAN, R. 1974 On Kolmogorov's inertial-range theories. *J. Fluid Mech.* **62**, 305–330.

KRISTENSEN, L., LENSCHOW, D. H., KIRKEGAARD, P. & COURTNEY, M. 1989 The spectral velocity tensor for homogeneous boundary-layer turbulence. *Boundary-Layer Met.* **47**, 149–193.

KUZNETSOV, V. R., PRASKOVSKY, A. A. & SABELNIKOV, V. A. 1992 Fine-scale turbulence structure of intermittent shear flows. *J. Fluid Mech.* **243**, 595–622.

LESIEUR, M. 1987 *Turbulence in Fluids*. Kluwer.

LIANDRAT, J. & MORET-BAILLY, F. 1990 The wavelet transform: some applications to fluid dynamics and turbulence. *Eur. J. Mech.* B/*Fluids* **9**, 1–19.

LUMLEY, J. L. 1970 *Stochastic Tools in Turbulence*. Academic.

MAHRT, L. 1991*a* Eddy asymmetry in the sheared heated boundary layer. *J. Atmos. Sci.* **48**, 472–492.

MAHRT, L. 1991*b* Eigen-structure of eddies; continuous weighting versus conditional sampling. In *Non-linear Variability in Geophysics* (ed. D. Schertzer & S. Lovejoy), pp. 145–156. Kluwer.

MAHRT, L. & FRANK, H. 1988 Eigen structure of eddy microfronts. *Tellus* **40A**, 107–119.

MAJDA, A. J. 1991 Vorticity, turbulence and acoustics in fluid flow. *SIAM Rev.* **33**, 349–388.

MALLAT, S. G. 1989 Multifrequency channel decompositions of images and wavelet models. *Trans. Acoustics, Speech Signal Proc.* **37**, 2091–2109.

MANDELBROT, B. B. 1976 Intermittent turbulence and fractal dimension: kurtosis and the spectral exponent $5/3+\beta$. In *Turbulence and Navier–Stokes Equations* (ed. R. Teman). Lecture Notes in Mathematics, vol. 565, pp. 121–145. Springer.

MENEVEAU, C. 1991 Analysis of turbulence in the orthonormal wavelet representation. *J. Fluid. Mech.* **232**, 469–520.

MOFFATT, H. K. 1984 Simple topological aspects of turbulent vorticity dynamics. In *Turbulence and Chaotic Phenomena in Fluids*, (ed. T. Tatsumi), pp. 223–230. Elsevier.

MORRISON, J. F. & BRADSHAW, P. 1991 Bursts and sources of pressure fluctuations in turbulent boundary layers. In *Eighth Symp. on Turbulent Shear Flows*, Vol. 1, pp. 211–216. Tech. Univ. of Munich.

MORRISON, J. F., SUBRAMANIAN, C. S. & BRADSHAW, P. 1992 Bursts and the law of the wall in turbulent boundary layers. *J. Fluid Mech.* **241**, 75–108.

NELKIN, M. & BELL, T. L. 1978 One-exponent scaling for very high-Reynolds-number turbulence. *Phys. Rev.* A **17**, 363–369.

NOVIKOV, E. A. & STEWART, R. W. 1964 Intermittency and dissipation fluctuation spectrum. *Izv. Akad. Nauk SSSR* **32**, 22–24.

OBOUKHOV, A. M. 1962 Some specific features of atmospheric turbulence. *J. Fluid Mech.* **13**, 77–81.

PIERREHUMBERT, R. T. & WIDNALL, S. E. 1982 The two- and three-dimensional instabilities of a spatially periodic shear layer. *J. Fluid Mech.* **114**, 59–82.

SAFFMAN, P. G. 1971 On the spectrum and decay of random two-dimensional vorticity distributions at large Reynolds number. *Stud. Appl. Maths* **50**, 377.

SIROVICH, L. 1987 Turbulence and the dynamics of coherent structures. Part I: Coherent structures. *Q. Appl. Maths* **45**, 561–571.

TENNEKES, H. 1976 Fourier-transform ambiguity in turbulence dynamics. *J. Atmos. Sci.* **33**, 1660–1663.

TENNEKES, H. & LUMLEY, J. L. 1972 *A First Course in Turbulence*. MIT Press.

TOWNSEND, A. A. 1976 *The Structure of Turbulent Shear Flow*. Cambridge University Press.

YAGLOM, A. M. 1966 Dependence of inertial subrange characteristics on dissipation fluctuations. *Dokl. Akad. Nauk SSSR* **166**, 49–52.

YAKHOT, V., SHE, Z.-S. & ORSZAG, S. A. 1989 Deviations from the classical Kolmogorov theory of the inertial range of homogeneous turbulence. *Phys. Fluids* A **1**, 289–293.

YAMADA, M. & OHKITANI, K. 1990 Orthonormal wavelet expansion and its application to turbulence. *Prog. Theor. Phys.* **83**, 819–823.

YAMAZAKI, H. 1990 Breakage models: lognormality and intermittency. *J. Fluid Mech.* **219**, 181–193.

YEUNG, P. K. & BRASSEUR, J. G. 1991 The response of isotropic turbulence to isotropic and anisotropic forcing at the large scales. *Phys. Fluids* A **3**, 884–897.